Formation of interfaces in bicontinuous phases

Michael W. Deem[1,2] and David Chandler[1]
[1]*Department of Chemistry and* [2]*Department of Chemical Engineering, University of California, Berkeley, California 94720*
(Received 12 January 1994)

With the charge-frustrated model, this paper examines the structure of interfaces in bicontinuous oil-water-surfactant phases. We analyze the nonlinear model by variational perturbation theory with a reference system that explicitly allows for interfaces. On the length scales consistent with a microscopic length cutoff, the theory predicts distinct microphase separation for some systems that have been considered bicontinuous. For other systems, for which experimentalists have imagined microphase separation but not bicontinuity, the theory predicts near homogeneity, i.e., highly diffuse interfaces.

PACS number(s): 82.70.Kj, 05.20.−y, 61.20.Gy, 61.25.Em

I. INTRODUCTION

Applying the charge-frustrated model, this paper develops conclusions concerning the nature of interfacial structure in bicontinuous phases. The charge-frustrated model is a nonlinear, field theoretic Hamiltonian for oil, water, and surfactant microemulsions [1–3]. The fields in this theory are the densities of the different components. The Hamiltonian predicts self-assembly [2]. For bicontinuous phases, an optimized Gaussian treatment of this nonlinear Hamiltonian seems justified [3]. In particular, the resulting parameters acquire physically reasonable values when the predictions of the theory in this approximation are fit to experimental small-angle neutron scattering (SANS) data. A Gaussian reference system, however, does not support thin interfaces. In this paper, we consider a reference system generated by a nonlinear yet local transformation of Gaussian fields. The procedure is based upon a variational principle. The parameters associated with the reference system allow the probability distribution for the oil or water densities at a given point in space to vary from the bimodal behavior expected for a microphase-separated system to the Gaussian behavior expected for a nearly homogeneous system. This treatment, therefore, allows us to address the issue of whether interfaces in a bicontinuous phase are sharp or diffuse. We will see that both possibilities exist, depending upon thermodynamic state conditions.

Landau-Ginzberg expansions have often been used to model microemulsion behavior [4]. The advantage of the charge-frustrated model is that the adjustable parameters involved have physical meaning in terms of quantities such as molecular lengths and pure oil-water surface tensions. Recently a single-component Landau-Ginzberg field theory has been analyzed by a lattice Monte Carlo simulation [5]. The simulations, while small scale, explore a variety of microemulsion phases, from lamellar to bicontinuous. These simulations agree with our analytical theory that bicontinuous phases with rather diffuse interfaces can occur.

Our approach of assuming there exist underlying Gaussian fields nonlinearly related to physical fields is not new. For example, clipped Gaussian models have been used to study phase separation due to spinodal decomposition [6] and microphase separation in microemulsions [7,8]. Transformed Gaussian functions have also been used to approximate the nonlinear time dependent Landau-Ginzburg equations for domain growth [9]. In these works, the transformation was chosen arbitrarily to be a step function [6–8] or sigmoidal function [9] so as to generate an extreme form of bimodality. Our approach employs a Hamiltonian based criterion for the transformation and need not lead to bimodal density distributions. The variational approach developed here should be applicable to a variety of systems currently of interest, from microphase-separated microemulsions to strongly segregated diblock copolymer melts.

In Sec. II we develop a theory for the variationally optimized clipped Gaussian reference system. We apply these results by comparing SANS data with the scattering curve resulting from the variationally optimized reference system for the nonlinear oil, water, and surfactant microemulsion Hamiltonian in Sec. III. We use a prediction of microphase separation from Sec. III to present typical real-space oil, water, and surfactant configurations in Sec. IV. We conclude in Sec. V.

II. THEORETICAL DEVELOPMENT

The nonlinear charge-frustrated Hamiltonian developed in Refs. [1,3] is of the following form:

$$\beta H[\boldsymbol{\rho}] = \sum_{i=1}^{4} \int d\mathbf{r} \frac{1}{n_i} \rho_i(\mathbf{r})[\ln \rho_i(\mathbf{r}) - 1] + \frac{1}{2(2\pi)^3} \int_{|\mathbf{k}|<k_c} d\mathbf{k}\, \delta\hat{\boldsymbol{\rho}}^{\top}(-\mathbf{k}) \hat{\mathbf{A}}(k) \delta\hat{\boldsymbol{\rho}}(\mathbf{k}) , \quad (1)$$

where

$$\hat{\mathbf{A}}(k) = \beta[(j + gk^2)\mathbf{D} + 4\pi z^2\, \mathbf{C}/k^2] . \quad (2)$$

Here the vector $\delta\boldsymbol{\rho}(\mathbf{r})$ has components $\rho_i(\mathbf{r}) - \rho_i$ for the density fluctuations of water ($i = 1$), surfactant head ($i = 2$), and surfactant tail segments ($i = 3$). There are only three independent densities since for long wavelengths, i.e., for $k < k_c$, we assume the oil density ($i = 4$) is related to these three densities by incompressibility. That is,

$$\rho_4(\mathbf{r}) = \rho_0 - \rho_1(\mathbf{r}) - \rho_2(\mathbf{r}) - \rho_3(\mathbf{r}) \ , \tag{3}$$

where ρ_0 is the total particle density of the fluid. The quantity n_i is the number of segments per component (e.g., n_2 is the number of waterlike, or head, groups in a surfactant molecule), the symmetric matrix $\mathbf{C}$ has elements $C_{22} = 1/n_2^2, C_{33} = 1/n_3^2, C_{23} = -1/n_2 n_3$, and zero otherwise, and the symmetric matrix $\mathbf{D}$ has elements $D_{11} = D_{22} = D_{12} = 1$ and zero otherwise.

The Hamiltonian (1) is of the form of a nonquadratic local term and quadratic nonlocal terms. Competition between these two terms leads to a variety of self-assembled bilayers and micelles in Monte Carlo calculations [2]. The electrostatic or Coulombic terms, which frustrate the underlying Ising system, arise from the constraints of surfactant stoichiometry. The magnitude of the frustrating charge is $z = (3/4\pi\beta\rho_s\Delta^2)^{1/2}$, where Δ is root-mean-square length separating head and tail groups in surfactant molecule and ρ_s is the bulk concentration of surfactant. The presence of the Coulombic terms leads to the characteristic peak in the scattering curve observed by SANS experiments when the Hamiltonian is treated by a variationally optimized Gaussian reference system [3].

A Gaussian reference system, however, cannot support thin interfaces and therefore cannot discern whether density profiles in a self-assembled system are sharp or diffuse. To address this physical issue, we propose the following reference system:

$$\rho_i(\mathbf{r}) = c_i[\phi_i(\mathbf{r}) + \phi_i^0], \qquad i = 1,2,3 \ , \tag{4}$$

where $c_i(x)$ is referred to as the transfer function and the fields $\phi_i(\mathbf{r})$ are taken to be Gaussian. The transfer function is required to be positive and typically would be expected to have a sigmoidal shape. The overall scale of the fluctuations in $\phi_i(\mathbf{r})$ then defines whether the clipping function is essentially a linear transform, a step function, or a smoothly varying sigmoidal function. That is, a small scale implies diffuse interfaces; conversely, a large scale implies sharp interfaces. The shift ϕ_i^0 is defined by the condition

$$\langle \rho_i(\mathbf{r}) \rangle_0 = \rho_i \ , \tag{5}$$

where the average $\langle\ \rangle_0$ is taken over the Gaussian fields $\boldsymbol{\phi}(\mathbf{r}) = [\phi_1(\mathbf{r}), \phi_2(\mathbf{r}), \phi_3(\mathbf{r})]$ with the distribution

$$P_0[\boldsymbol{\phi}(\mathbf{r})] \propto \exp\{ -\beta H_0[\boldsymbol{\phi}(\mathbf{r})]\} \tag{6}$$

and

$$\beta H_0[\boldsymbol{\phi}(\mathbf{r})] = \frac{1}{2(2\pi)^3} \int_{|\mathbf{k}|<k_c} d\mathbf{k}\ \hat{\boldsymbol{\phi}}^{\top}(-\mathbf{k})[\hat{\boldsymbol{\chi}}^{(0)}(k)]^{-1}\hat{\boldsymbol{\phi}}(\mathbf{k}) \ . \tag{7}$$

The spectrum $\hat{\boldsymbol{\chi}}^{(0)}(k)$ in Eq. (7) depends only on $|\mathbf{k}|$ just as $\hat{\mathbf{A}}(k)$ in Eq. (1) depends only on $|\mathbf{k}|$ in an isotropic fluid. Note that the positivity of c_i does not guarantee that $\rho_4(\mathbf{r})$ generated from the incompressibility condition will be positive. A treatment more complete than we are proposing here would incorporate four independent fields and require that incompressibility is satisfied only at $\mathbf{k} = \mathbf{0}$.

The Gibbs-Bogoliubov-Feynman variational bound can be used determine the unknown clipping function c_i and the Gaussian statistics of ϕ_i [10]:

$$\ln Z \geq \ln Z_0 - \beta\langle H[\boldsymbol{\rho}] - H_0[\boldsymbol{\phi}]\rangle_0 \ , \tag{8}$$

where

$$Z = \int \mathcal{D}[\boldsymbol{\rho}(\mathbf{r})] \exp\{-\beta H[\boldsymbol{\rho}(\mathbf{r})]\} \tag{9}$$

and

$$Z_0 = \int \mathcal{D}[\boldsymbol{\phi}(\mathbf{r})] \exp\{-\beta H_0[\boldsymbol{\phi}(\mathbf{r})]\} \ . \tag{10}$$

Implementation of the variational principle implied by Eq. (8) requires expressing $H[\boldsymbol{\rho}(\mathbf{r})]$ in terms of $\boldsymbol{\phi}(\mathbf{r})$. The result of this change of variables gives a Hamiltonian for $\boldsymbol{\phi}(\mathbf{r})$

$$\beta H'[\{\phi_i(\mathbf{r})\}] = \beta H(\{c_i[\phi_i(\mathbf{r})]\}) - \frac{1}{v}\sum_{i=1}^{3}\int d\mathbf{r} \ln \partial c_i/\partial\phi_i(\mathbf{r}) \ , \tag{11}$$

where the last term comes from the Jacobian of the transformation. The volume element is $v = \epsilon^3$, where ϵ is a grid spacing. Fluctuations on length scales smaller than ϵ are not resolved. The volume element v can be identified as

$$v = \frac{6}{\pi}\left(\frac{\pi}{k_c}\right)^3 \tag{12}$$

by the requirement that a linear change of variables in a Gaussian field theory leave the partition function (10) invariant. Essentially this calculation entails equating the volume in k space associated with a lattice ($8\pi^3/v$) to that associated with a spherical cutoff ($\frac{4}{3}\pi k_c^3$).

Denoting the density-density correlation function by

$$\chi_{ij}(|\mathbf{r} - \mathbf{r}'|) = \langle \delta\rho_i(\mathbf{r})\delta\rho_j(\mathbf{r}')\rangle_0 \ , \tag{13}$$

the function to be minimized is given by

$$E = F + \frac{1}{2V}\sum_{\mathbf{k}}\left(\sum_{ij}\hat{\chi}_{ij}(k)\hat{A}_{ij}(k) - \ln\det\hat{\boldsymbol{\chi}}^{(0)}(k)\right) . \tag{14}$$

Here V denotes the system volume and the function F contains the average of the nonquadratic local terms in $\beta H'$:

$$F[\chi_{ij}^{(0)}(0)] = \sum_{i=1}^{4}\langle \rho_i(\mathbf{r})[\ln\rho_i(\mathbf{r}) - 1]\rangle_0/n_i - \frac{1}{\Delta}\sum_{i=1}^{3}\langle \ln[\partial c_i/\partial\phi_i(\mathbf{r})]\rangle_0 \ . \tag{15}$$

Note that, as indicated, F can depend only on $\chi_{ij}^{(0)}(r=0)$ given the Hamiltonian (7). This functional (14) should be minimized with respect to the functions $\hat{\chi}_{ij}^{(0)}(k)$ and the functions $c_i(\phi_i)$.

The functional minimization of Eq. (14) with respect to $\hat{\chi}_{ij}^{(0)}(k)$ is difficult due to the complicated relationship between $\hat{\chi}_{ij}(k)$ and $\hat{\chi}_{ij}^{(0)}(k)$ implied by Eqs. (4) and (13). In our numerical work, however, we have observed that for bulk correlations, the functions $\hat{\chi}_{ij}(k)$ and $\hat{\chi}_{ij}^{(0)}(k)$ are roughly proportional at small k. This proportionality holds for microemulsion bulk SANS data. Given this fact, the proportionality constant is given by the coefficient of the leading term in the expansion of $\chi_{ij}(r)$ in terms of $\chi_{ij}^{(0)}(r)$ as

$$\chi_{ij}(r) = \gamma_i\gamma_j\chi_{ij}^{(0)}(r) + \cdots , \tag{16}$$

where

$$\gamma_i = \gamma_i[\chi_{ii}^{(0)}(0)] = \langle \partial c_i/\partial\phi_i\rangle_0 . \tag{17}$$

The terms omitted from Eq. (16) are of the order of $[\chi_{ij}^{(0)}(r)/\chi_{ij}^{(0)}(0)]$ smaller than those retained, and expansion (16) is valid at large r where the correlation function decays. Expansion (16) provides an explanation for the observation that $\hat{\chi}_{ij}(k)$ and $\hat{\chi}_{ij}^{(0)}(k)$ can be roughly proportional at small k. It is an accurate approximation for bulk correlation functions (as opposed to surface or interface correlations), and we will limit its application to such cases.

With this simplification, Eq. (14) becomes

$$E = F + \frac{1}{2V}\sum_{\mathbf{k}}\left(\sum_{ij}\gamma_i\gamma_j\hat{\chi}_{ij}^{(0)}(k)\hat{A}_{ij}(k) - \ln\det\hat{\boldsymbol{\chi}}^{(0)}(k)\right). \tag{18}$$

Implementing the condition

$$\partial E/\partial\hat{\chi}_{ij}^{(0)}(\mathbf{k}) = 0 \tag{19}$$

leads to the relation

$$\hat{\chi}_{ij}^{(0)^{-1}}(k) = \alpha_{ij} + \gamma_i\gamma_j\hat{A}_{ij}(k) + \frac{2\delta_{ij}}{(2\pi)^3}\frac{d\gamma_i}{d\chi_{ii}^{(0)}}\sum_\ell\gamma_\ell\int d\mathbf{k}\;\hat{A}_{i\ell}(k)\hat{\chi}_{i\ell}^{(0)}(k) , \tag{20}$$

where

$$\alpha_{ij} = \frac{dF}{d\chi_{ij}^{(0)}} + \frac{dF}{d\chi_{ji}^{(0)}} . \tag{21}$$

Note that the total derivatives in Eqs. (20) and (21) involve partial derivatives with respect to ϕ_i^0 due to the constraint (5). It is to be understood that the summation and integration over $\mathbf{k}$ in Eqs. (18) and (20) are confined to $k < k_c$. Indeed, without a cutoff, $\chi_{ij}^{(0)} = \chi_{ij}^{(0)}(r=0)$ would be infinite.

Equation (20) is an integral equation for the correlation function of the variationally optimized transformed-Gaussian reference system. Essentially, the inverse spectrum of the variationally optimized reference system is a constant times that in the original Hamiltonian plus another constant, with the constants determined self-consistently. Note that Eq. (20) reproduces the variationally optimized Gaussian reference system of our prior paper [3] when the transfer function is linear.

Equation (20) can be solved by a globally convergent modification of Newton's method [11] applied to Eqs. (17) and (21). The region of convergence (i.e., the basin of attraction) around the solution is exceedingly small, however, when $\hat{\chi}_{ij}(k)$ has the form typical of microemulsion SANS data. This feature implies the parameters associated with βH must be varied only in small increments if the root-finding algorithm is to converge on Eqs. (17) and (21). The F function of Eq. (15) contains three one-dimensional integrals due to single-site averages associated with $\rho_1(\mathbf{r})$, $\rho_2(\mathbf{r})$, and $\rho_3(\mathbf{r})$ and one three-dimensional integral due to the three-site average associated with $\rho_4(\mathbf{r})$. The single-site averages were done to a specified tolerance by adaptive Gauss-Legendre integration and the multi-site average was done by 20th-order Gauss-Legendre integration [12]. For consistency with our companion paper [3], the $\rho_i(\mathbf{r})\ln\rho_i(\mathbf{r})$ in F were expanded to fourth order in $\delta\rho_i(\mathbf{r})$ about ρ_i before the averages were taken. The γ_i were also determined by adaptive Gauss-Legendre integration, as was the ϕ_i^0 implicitly defined by Eq. (5).

III. RESULTS AND DISCUSSION

We have fit the variationally optimized transformed-Gaussian reference system to bulk-contrast SANS data taken for several typical microemulsion systems [6–9]. That is, the sum of the residuals squared ($\mathcal{S}$), given by

$$\mathcal{S} = \frac{1}{2}\sum_j[i_{\rm obs}(k_j) - f\chi_{11}(k_j)]^2 , \tag{22}$$

was minimized with respect to the parameters in βH for the measured SANS intensity $i_{\rm obs}(k)$. The wave vectors k_j were chosen uniformly in the small-angle region as in our companion paper [3]. The scale factors f are calculable in all these experiments [3]. However, as in Ref. [3], we will take f as an adjustable parameter. The variability in f is then one measure of the accuracy of our approach. The correlation function $\hat{\chi}_{11}(k)$ is generated from the relation $\hat{\chi}_{11}(k) = \gamma_1^2\hat{\chi}_{11}^{(0)}(k)$. In order to apply Eq. (20), the form of $c_i(x)$ is required. We chose

$$c_i(x) = c(x) = \frac{\rho_0}{2}[1+\tanh(x)] . \tag{23}$$

In a seemingly more general choice of $c_i(x) = (\rho_0/2)[1+\tanh(\lambda_i x)]$, the parameter λ_i is irrelevant since this choice coincides with a linear transformation of the fields $\phi_i(\mathbf{r})$. The transfer function (23) ensures that $\rho_1(\mathbf{r})$, $\rho_2(\mathbf{r})$, and $\rho_3(\mathbf{r})$ are positive and leads to values of $\rho_4(\mathbf{r})$ generated by the incompressibility condition that are usually positive. Tables I and II list the results of our fit of the parameters j and g when βH is treated by the variationally

TABLE I. The results of fitting the model Hamiltonian Eq. (1) to the SANS data of Ref. [15]. Only the data for the 1-octanol cosurfactant were fit. Both the variationally optimized Gaussian reference system (VG) [3] and the variationally optimized transformed Gaussian reference system (VTG) parameters are indicated. The energy units are k_BT and the length units are Å, except for f_{VG} and f_{VTG}, which have units of Å^3/cm. Calculations done with cutoff wave vector $k_c = 0.15$ Å^{-1}.

$\rho_2+\rho_3$	ρ_1	ρ_4	n_1	n_2	n_3	n_4	Δ	f_{VG}	g_{VG}	j_{VG}	f_{VTG}	g_{VTG}	j_{VTG}
0.010667	0.008333	0.014333	1	1	10	15	8.0	7.13	768	-298	10.8	820	-335
0.011333	0.006667	0.015333	1	1	10	15	8.0	9.77	957	-359	14.3	975	-454
0.011667	0.005667	0.016	1	1	10	15	8.0	11.75	1043	-399	15.8	1180	-612
0.012333	0.004667	0.016333	1	1	10	15	8.0	9.38	1262	-436	12.1	1560	-740

optimized Gaussian [3] and transformed-Gaussian reference systems. Due to the small basin of attraction and the resulting difficulty in finding convergence to Eq. (20), the parameters that minimize Eq. (22) were determined by hand for the transformed Gaussian case. The quality of the fits is roughly that of our preceding paper [3], however.

The form on the transfer function Eq. (23) was chosen to allow the possibility of bimodal distributions in the point densities of oil and water in the Hamiltonian (1). We let $p_i(\rho)$ denote the probability distribution that the density $\rho_i(\mathbf{r})$ at position $\mathbf{r}$ has the value ρ, a quantity independent of $\mathbf{r}$ in this translationally invariant system. Figures 1–3 present these density distributions for water as predicted by the variationally optimized Gaussian and transformed Gaussian cases. The pure Gaussian case results simply in

$$p_i(\rho) = [2\pi\chi_{ii}(0)]^{-1/2} \exp[-(\rho-\rho_i)^2/2\chi_{ii}(0)] \; . \quad (24)$$

The transformed Gaussian results in a modified distribution

$$p_i(\rho) = [2\pi\chi_{ii}^{(0)}(0)]^{-1/2} \exp[-\phi_i^2/2\chi_{ii}^{(0)}(0)] \; \frac{1}{\partial c/\partial\phi_i}, \quad (25)$$

where $\rho = c(\phi_i + \phi_i^0)$ and $c(x)$ is given by Eq. (23). It is immediately obvious that the transformed-Gaussian reference system leads to densities that more nearly obey the constraints real densities do than does the Gaussian reference system. For example, the water site density is always positive in the transformed-Gaussian reference system. The Gaussian reference system predicts large fluctuations in the water site density, and the resulting large width in the probability distribution leads to negative densities occurring with significant probabilities. Such negative densities are clearly unacceptable in a quantitatively accurate density field theory. These negative densities lead to distortions in the predicted $\chi_{ij}(r)$ and can lead to such results as a negative radial distribution function $g_{ij}(r)$, which is impossible in any real physical system [13]. A transformed-Gaussian reference system alleviates such difficulties (with the proviso that incompressibility be treated correctly as a condition only at $\mathbf{k} = \mathbf{0}$).

More striking is the shape of the $p_i(\rho)$ curves in Figs. 1 and 2 for the transformed-Gaussian reference system. While they are certainly distinct from the Gaussian distributions, in no case are they highly bimodal. In fact, neither of these systems was postulated to be bicontinuous, although Ref. [14] suggested freeze-fracture evidence for microphase separation. Figure 1(a), which corresponds to a scattering curve that peaks at the smallest k, is the only case in which a degree of bimodality occurs. Intuitively, one expects the degree of mixing to increase and the degree of bimodality to decrease as the characteristic domain size of the microemulsion decreases. This result is expected due to the increased role of interfacial fluctuations on small domains. In other words, a microemulsion can only microphase separate when the microphases are of a significant size. This trend of decreasing bimodality is observed in Figs. 1(a)–1(d), where the degree of bimodality decreases as the position of the SANS peak shifts to a larger inverse distance. The degree of mixing is also expected to increase and interfaces to broaden as the concentration of surfactant is increased beyond that which can be accommodated at a sharp, albeit complicated, interface. Figure 2 indeed indicates a complete lack of bimodality for a system with a very high surfactant concentration.

Bear in mind that the length scales resolved in our theory are those that are larger than $v^{1/3}$ separated, but the typical distances across a local oil- or water-rich region are of the order of or smaller than $v^{1/3} \sim 30$ Å. In such a case, the probability $p_i(\rho)$ would be unimodal.

The experimental $i(k)$ corresponding to Figs. 1 and 2 roughly satisfy a sum rule implied for a microphase-separated system with a highly bimodal site density distribution. That is, $\chi_{11}(r=0) \leq \rho_1(\rho_0 - \rho_1)$, and equality is achieved if the system is highly bimodal. (Actually this sum rule applies to data that have been smoothed with

TABLE II. The results of fitting the model Hamiltonian Eq. (1) to bicontinuous SANS data. The energy units are k_BT and the length units are Å, except for f_{VTG}, which has units of Å^3/cm.

$\rho_2+\rho_3$	ρ_1	ρ_4	n_1	n_2	n_3	n_4	Δ	f_{VTG}	g_{VTG}	j_{VTG}
0.017333[a]	0.008	0.008	1	7.2	9.6	8	10.0	447.8	4840	-104
0.004667[b]	0.014333	0.014333	1	4	16	6	8.0	4.6	992	-157

[a] A fit to SANS data of Ref. [16]. The wave vector cutoff used in the calculations is $k_c = 0.15$ Å^{-1}.
[b] A fit to SANS data of Ref. [17]. The wave vector cutoff used in the calculations is $k_c = 0.10$ Å^{-1}.

a filter to remove the high-k molecular details from the scattering curve. Such a filter would have a vanishing effect on the small-k data measured by SANS, which additionally decay as k^{-4} for intermediate k.) In fact these experimental data imply that $\chi_{11}(0)$ is somewhat larger than $\rho_1(\rho_0-\rho_1)$, indicating that perfect contrast was not achieved in these SANS experiments. Our treatment of the model Hamiltonian (1), however, satisfies the bound $\chi_{11}(0) < \rho_1(\rho_0-\rho_1)$ and fitting the experimental data with $\hat{\chi}_{11}(k)$ requires values of f that are two or three times too large. For example, had perfect contrast been achieved for the data reported in Ref. [15], f would be 4.2 Å^3/cm. To fit this data, we required $f \sim 10$ Å^3/cm (see Table I). This difference is perhaps a matter of detail which might be clarified with further experimental work focusing on the contrast matching and with a more complete treatment of the charge frustrated model that allows for more than just two energy parameters.

For the data in Ref. [16], however, the difference may be far more significant and seems to deserve more attention both theoretically and experimentally. In the case of Ref. [16], assumption of perfect contrast yields $f = 3.7$ Å^3/cm, while the transformed-Gaussian treatment of the Hamiltonian (1) requires $f \approx 400$ Å^3/cm to fit that data (see Table II). Assuming that there is no error in the reported experimental scale, we must conclude that the

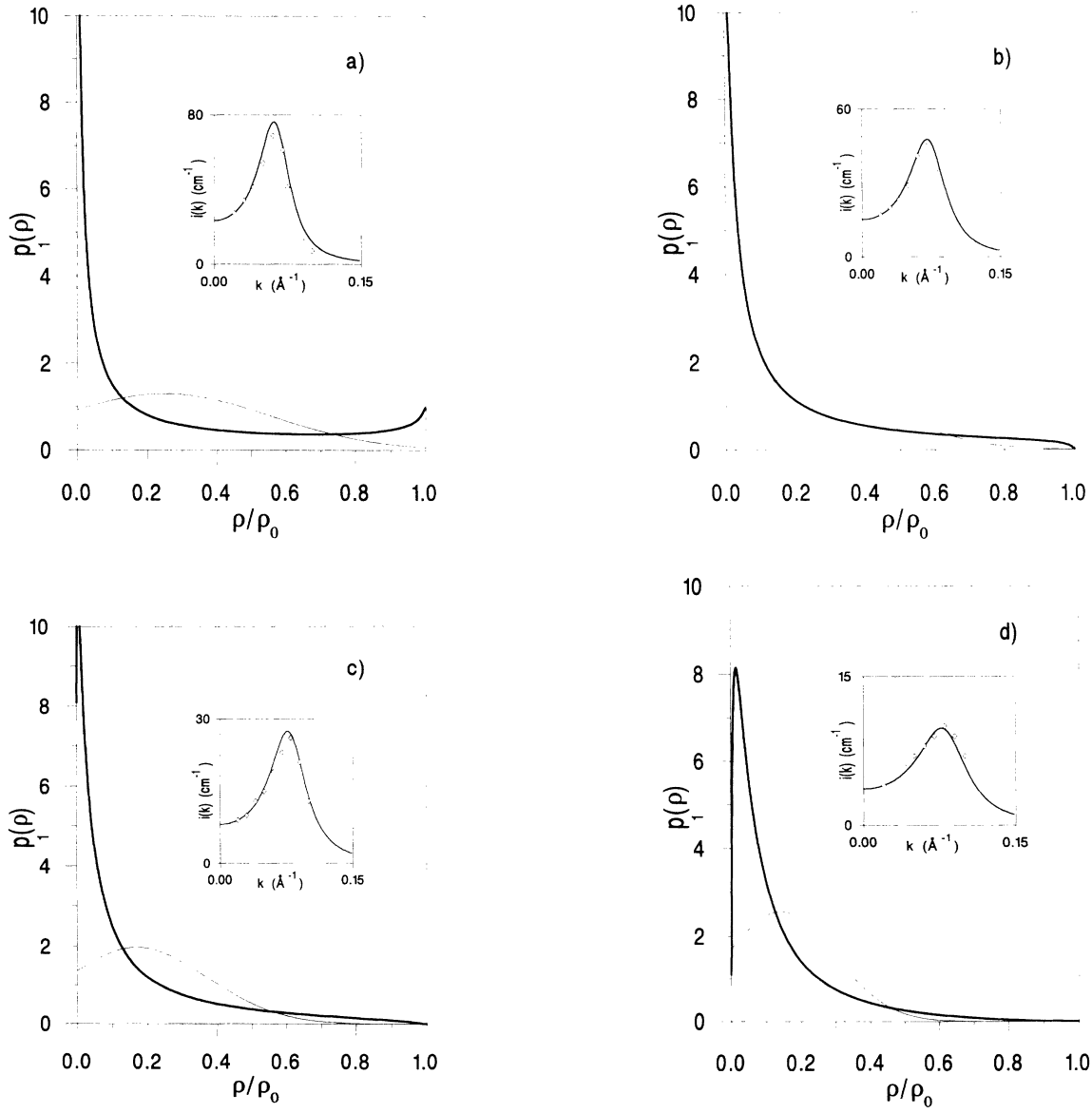

FIG. 1. Single-site probability distributions for the water density [denoted by $p_i(\rho)$] for the variationally optimized Gaussian (thin line) and the variationally optimized clipped Gaussian (thick line) treatments. (a)–(d) correspond to the first through fourth fits listed in Table I. The density ρ_0 is 1/ 30 Å^3. In the clipped theory, $\rho_1(\rho)$ is properly zero outside the pictured range $0 < \rho < \rho_0$. In the Gaussian theory, the Gaussian $\rho_1(\rho)$ is, at least to some extent, nonzero outside that region. The insets depict comparisons of the bulk scattering curves predicted by the transformed-Gaussian treatment with those measured by SANS (diamonds).

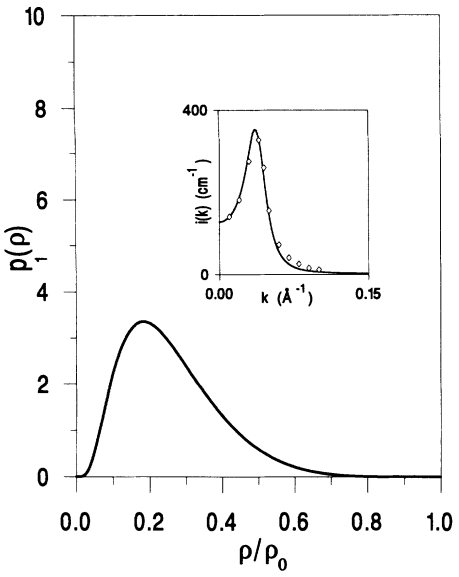

FIG. 2. Single-site probability distributions for the water density [denoted by $p_i(\rho)$] for the variationally optimized clipped Gaussian treatment corresponding to the first fit in Table II. The density ρ_0 is 1/30 Å^3. The inset depicts a comparison of the bulk scattering curve predicted by the transformed-Gaussian treatment (thick line) with that measured by SANS (diamonds).

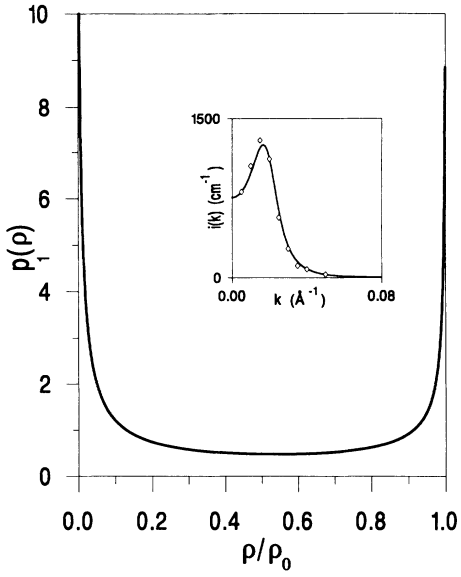

FIG. 3. Single-site probability distributions for the water density [denoted by $p_i(\rho)$] for the variationally optimized clipped Gaussian treatment corresponding to the second fit in Table II. The density ρ_0 is 1/30 Å^3. The inset depicts a comparison of the bulk scattering curve predicted by the transformed-Gaussian treatment (thick line) with that measured by SANS (diamonds).

theoretical model predicts density fluctuations that are far too small for this particular system. Indeed, in the model with only two j and g parameters, density fluctuations cannot be very large at the high surfactant concentrations considered in Ref. [16] (see also Ref. [3]). The resulting near-Gaussian behavior of the density predicted by the model for this system is evident in Fig. 2.

In contrast, we can find bimodality for bicontinuous phases where the experimental microemulsion SANS data show a peak at smaller k than do those of Refs. [15,16]. Figure 3 indicates the results of a variationally optimized transformed-Gaussian calculation for such a situation. The surfactant interface was studied by contrast matching in Ref. [17], and the mean curvature of the interface was shown to be zero. Such a result is entirely consistent with a bicontinuous structure. Figure 3 clearly supports such a conjecture. Note that we predict bimodality even though our fit value of f is somewhat larger than the expected value of 2.5 Å^3/cm.

The authors of Ref. [18] suggest that their SANS data is from a disordered bicontinuous phase as well. We have found these data to be extremely difficult to fit with the variationally optimized transformed-Gaussian procedure. The region of convergence for Eq. (20) is particularly small in this case, and the efficiency of the algorithm we use to solve this equation diminishes as the region of convergence shrinks. We have carried the calculation far enough to successfully fit the peak position of the SANS structure factor. The resulting parameters lead to a highly bimodal density distribution similar to that presented in Fig. 3. A markedly bimodal density distribution is consistent with the low surfactant concentration in the system [allowing Eq. (25) to show bimodality with only a moderate $\chi_{11}^{(0)}(0)$] and with the experimental data that reasonably satisfy $\chi_{11}(0) \cong \rho_1(\rho_0 - \rho_1)$.

The oil-water surface tension associated with Hamiltonian (1) applied to a phase-separated oil and water mixture (in the absence of surfactant) can be calculated in a mean-field approximation [19]. We have described this standard calculation for this particular context in Ref. [3]. We have carried out the calculations for j and g parameters listed in Table I. We find surface tensions in the range 0.17–0.28 k_BT/Å^2 with the j's and g's arrived at through the Gaussian treatment [3]. We find surface tensions in the range 0.19–0.43 k_BT/Å^2 for the j's and g's arrived at through the transformed-Gaussian treatment. The surface tensions obtained from the parameters in Table II are in a similar range. A typical oil-water surface tension is 0.12 k_BT/Å^2 [20]. Given that the transformed-Gaussian treatment is expected to be the more accurate of the two, it appears fortuitous that the Gaussian treatment leads to a more accurate surface tension. In fact, one should not expect a water, oil, and surfactant mixture should be described by only two energy parameters j and g. There should be a whole matrix of such terms [3]. The simplified assumption of only two parameters is what leads to the only approximately correct surface tension deduced above.

Along with surface tension, the mean-field approximation also predicts interfacial widths. With the parameters listed in Tables I and II, this approach generally predicts interfacial widths of oil-water interfaces to be roughly 10 Å. The parameters found to fit the scattering data of Ref. [16], however, lead to a rather large width of 50 Å

for the oil-water interface in the absence of surfactant. Such a large width in the pure oil and water system is, of course, consistent with the predicted lack of bimodal behavior in the microemulsion.

With the aid of a mean-field model, one may attempt to estimate an intrinsic oil-water interfacial width in the presence of surfactant, i.e., for the bicontinuous microemulsion. Specifically, we use

$$p_i(\rho) \approx \frac{1}{L}\int_{-L/2}^{L/2} dz\ \langle \delta[\rho - \rho_i(z)]\rangle$$

$$\approx \frac{1}{L}(dz/d\rho)\ . \tag{26}$$

Here the length L is the typical separation between the centers of oil-rich and water-rich regions for a microphase separated system. A reasonable value is $L \sim \pi/k_{\max} \sim 10^2$Å, where $k_{\max}$ is the wave vector at which $i(k)$ is maximum. For the system considered in Fig. 3, the solution of the differential equation (26) is shown in Fig. 4. The broad interfacial profile pictured there must be the result of an extremely small effective surface tension (if that property is defined). Indeed, consider the total surface area A separating microregions of oil from those of water. Since the correlation length of the bicontinuous phase is finite, one might argue that this total surface area grows linearly with system size. Our transformed-gaussian treatment, in fact, predicts the surface area is extensive (see also Fig. 5). As such, the average surface area is that which minimizes the free energy F. Hence $\partial F/\partial A = 0$. In other words, the persistence of microphase separated structures throughout a bicontinuous system implies that the surfactant has induced zero surface tension between oil and water.

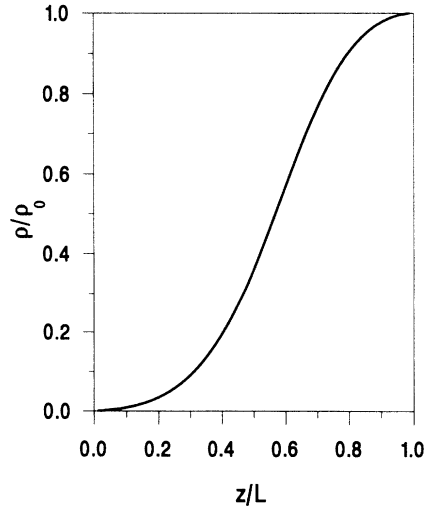

FIG. 4. The average interfacial density profile predicted using Eq. (26) for the system corresponding to the second fit of Table II.

IV. REAL-SPACE IMAGES

Our transformed Gaussian reference system is very similar to previous random wave [6–8] and transformed Gaussian [9] reference systems. Real-space images appear frequently in those works. We describe below an efficient method for generating real-space microemulsion configurations from our transformed Gaussian reference system.

The field theoretic Hamiltonian Eq. (7) provides a well defined probability for any given field configuration, Eq. (6). This distribution can be used to display typical density configurations that will occur in the ensemble. Specifically, the quadratic Hamiltonian in Eq. (7) can be written for a finite volume V as

$$\beta H_0 = \mathbf{b}\cdot\hat{\boldsymbol{\phi}}(\mathbf{0}) + \frac{1}{V}{\sum_{\mathbf{k}}}'\hat{\boldsymbol{\phi}}^{\top}(-\mathbf{k})[\hat{\boldsymbol{\chi}}^{(0)}(\mathbf{k})]^{-1}\hat{\boldsymbol{\phi}}(\mathbf{k})\ , \tag{27}$$

where the primed summation is over half of k space with $k < k_c$ and $\mathbf{b}$ is used to set average field values.

When specialized to a one-component field by integrating out all field components but one $\phi_i(\mathbf{r})$ such a Hamiltonian predicts that all the Fourier components, real and imaginary parts, in "half" of k space are independent, Gaussian random variables, with a variance $V\hat{\chi}_{ii}^{(0)}(k)/2$. The other half of k space is defined by the relation $\hat{\phi}_i(-\mathbf{k}) = \hat{\phi}_i^*(\mathbf{k})$. There are, however, several special points in k space where, due to the constraints of reality of $\phi_i(\mathbf{r})$ and of translational symmetry, $\hat{\phi}_i(\mathbf{k})$ is required to be real. If the grid is numbered by $(-N_x/2+1, -N_y/2+1, -N_z/2+1)-(N_x/2, N_y/2, N_z/2)$, these special points are the eight points given by (0 or $N_x/2$, and 0 or $N_y/2$, 0 or $N_z/2$). The (real) Fourier components at each of these locations has variance $V\hat{\chi}_{ii}^{(0)}(\mathbf{k})$. The linear $k = 0$ term in Eq. (27) simply specifies the average field values, implying

$$\langle\hat{\phi}_i(\mathbf{0})\rangle = -V\sum_j \hat{\chi}_{ij}^{(0)}(\mathbf{0})b_j \tag{28}$$

and

$$\langle\hat{\phi}_i(\mathbf{k})\rangle = 0, \quad \mathbf{k}\neq\mathbf{0}.$$

The method of generating a typical configuration given the Hamiltonian Eq. (27) is thus clear. Fourier components are generated on a grid in half of k space by assigning Gaussian random variables to each grid point. The real-space density configuration is generated by performing a Fourier inversion,

$$\phi_i(\mathbf{r}) = \frac{1}{V}\sum_{\mathbf{k}}\hat{\phi}_i(\mathbf{k})e^{-i\mathbf{k}\cdot\mathbf{r}}\ , \tag{29}$$

where the sum is truncated at a wave vector corresponding to the discrete grid for visualization in real space.

The process can be optimized further by simply assigning Gaussian random variables with standard deviation $[\hat{\chi}_{ii}^{(0)}(k)/2V]^{\frac{1}{2}}$ to the real and imaginary parts of the Fourier components on half of a grid in k space, generating the other half of k space, and using a fast Fourier

transform to accomplish the sum over k space in Eq. (29) [21]. This operation of generalizing a typical configuration is very efficient and is $O(N^3 \ln^3 N)$ for a $N \times N \times N$ grid.

Figure 3 indicates that the water density is highly bimodal for the system of Ref. [17]. As such, we can choose $\rho_1(\mathbf{r}) = \rho_0$ if $\phi_1(\mathbf{r}) > 0$ and zero otherwise for display purposes. This essentially is choosing the transfer function to be a Heaviside function. Figure 5 presents a three-dimensional image of the dividing surface of a typical configuration generated in this fashion. The surface displayed is the level surface $\rho_1(\mathbf{r}) = \rho_4(\mathbf{r})$. Within the spirit of our model, this surface represents the layer of surfactant separating the bicontinuous phases oil and water phases. There are clearly many interesting topological features in this bicontinuous configuration. On long length scales, the behavior is random, but on shorter length scales, regions of a single, connected phase are clearly present. Of course, surface elastic moduli can be extracted from such configurations [8]. Figure 6 depicts a two-dimensional slice of this three-dimensional configuration. This configuration is remarkably similar to the real-space results of freeze-fracture TEM [14,22].

The domains observed in Fig. 5 have a large variety of shapes, with many narrow necks evident in the local domains of oil and water. Recall that a large wave vector cutoff k_c is intrinsic to the long-wavelength Hamiltonian (11) and implies a finite grid. The elemental length of the grid in Fig. 5 is 30 Å. To quantify the degree of constriction, we have computed the number of elemental cells that are adjacent to the interface on that grid. The number represents 45% of the total.

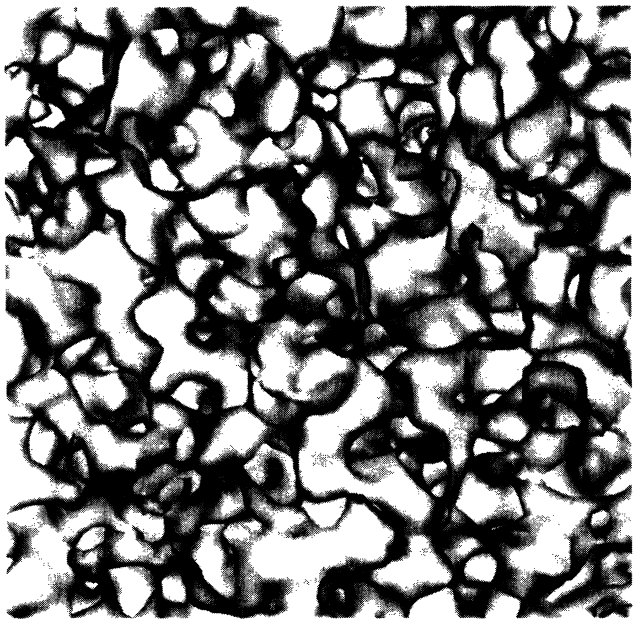

FIG. 5. The three-dimensional level surface $\rho_1(\mathbf{r}) - \rho_4(\mathbf{r})$ is visualized for the second parameter set of Table II. The view is along the z axis of a $64 \times 64 \times 64$ grid with 30 Å resolution.

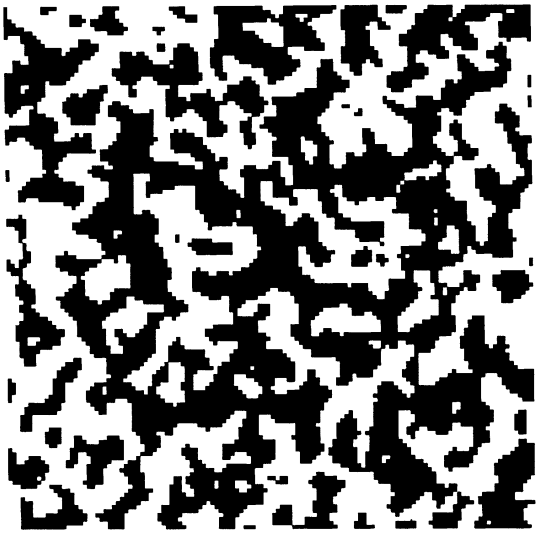

FIG. 6. The density field $\rho_1(\mathbf{r}) - \rho_4(\mathbf{r})$ is visualized for the second parameter set of Table II. The $z = 0$ slice of a $128 \times 128 \times 128$ grid with 30 Å resolution is presented.

V. CONCLUSIONS

In summary, this paper presents a treatment of a nonlinear Hamiltonian for oil, water, and surfactant microemulsions that can discern the differences between thin and diffuse interfaces. The theory is restricted, however, to length scales greater than $1/k_c$. When applied to SANS data that had been thought to be from microphase separated but not bicontinuous systems, the variationally optimized, transformed-Gaussian reference system indicates a lack of distinct bimodal behavior. This result, along with the failure of these experimental SANS data to satisfy a sum rule for bimodal distributions, indicates that some of the microemulsion systems examined by SANS may be closer to homogeneity than previously expected. When applied to SANS data that were postulated to be from bicontinuous phases, however, the nonlinear treatment predicts marked bimodal behavior. Real-space configurations generated from the Hamiltonian are strikingly similar to experimental freeze-fracture results.

A rough phase diagram of the behavior of our predicted $i(k)$ is indicated in Fig. 7. For given concentrations and surfactant lengths, we predict monotonically decaying scattering curves, peaked scattering curves, or lamellar phases (finite-k divergence in the scattering curve) in the j-g plane. Additionally, interfacial thickness within the peaked scattering curve region increases with increasing surfactant concentration. The Lifshitz line separating peaked and unpeaked scattering curves is given by the condition $\partial^2 \hat{\chi}_{11}(k)/\partial k^2 = 0$ at $k = 0$, and the instability lines separating the random and lamellar microemulsion phases is given by the first instance of $\hat{\chi}_{11}(k) \to \infty$ at k coinciding with the main peak in $\hat{\chi}_{11}(k)$. These transitions, as well as quantities such as peak positions, of course, follow once j and g are specified in the charge

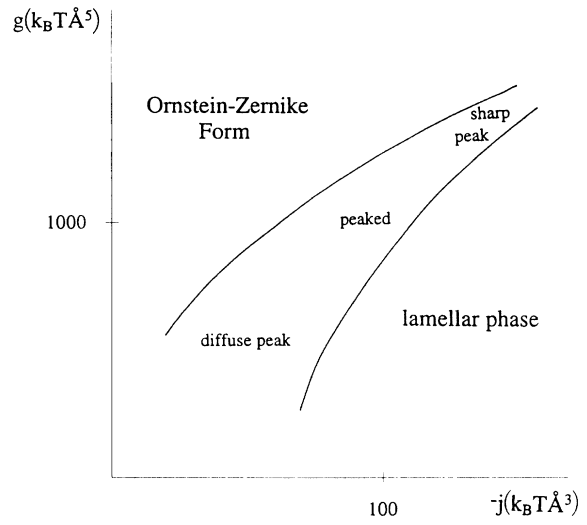

FIG. 7. Predicted phase diagram for the form of $i(k)$ in our j and g variables. Typical numerical values of j and g are indicated for the surfactant systems considered herein.

frustrated model.

The quantity $-j$ has the physical meaning of the unfavorable oil-water contact energy times the volume of a surfactant segment. The ratio of parameters g/j coincides roughly with the cross section of a surfactant segment. As such, these quantities could be adjusted independently within an experiment by varying, for example, the size of the molecules. Systematic SANS or small-angle x-ray scattering explorations of the phase diagram for various microemulsion constituents should map onto Fig. 7. Our predicted increasing diffuseness of the surfactant interface with increasing surfactant concentration is, of course, straightforward to study. *In situ* experiments such as NMR and high-k scattering experiments that probe the local molecular environment and thus provide information about the site density distributions in these systems should provide more comprehensive information about the bimodal character of these oil, water, and surfactant phases.

Our conclusions concerning interfaces are inferred from our examination of the local probability distribution $p_1(\rho)$. More direct examination requires extensions of the calculations presented here. Specifically, the treatment of correlations associated with surfactants confined to thin interfaces require corrections to the proportionality approximation Eq. (16). We have avoided these corrections in the current work as a matter of computational convenience. For the cases where $p_1(\rho)$ are bimodal, one may instead assume simply that the surfactant is confined to a molecularly thin oil-water interface. That assumption allows the surfactant correlation function to be computed in terms of $\hat{\chi}^{(0)}(k)$, as detailed, for example, by Teubner [8]. Since our computed bulk scattering curves agree with experiment, this hybrid procedure will agree with film scattering experiments for the cases of microphase separation [8].

Having established that the charge-frustrated model does successfully predict mesoscopic self-assembly with physically reasonable parameters, it would now be profitable to consider reduced representations of that model. For example, a one-component field theory should be derivable by integrating out surfactant fluctuations. The energies in that field theory will then be determined in terms of quantities such as surfactant length and concentrations. This approach may aid in the derivation of phase diagrams for the charge-frustrated model. It may also lead to molecular based predictions of the phenomenological parameters currently employed to interpret the behavior of self-assembled systems.

ACKNOWLEDGMENTS

This research has been supported by the NSF. M.W.D. thanks the Fannie and John Hertz Foundation for financial support. The field theory visualization was performed in the UCB College of Chemistry Graphics Center, with the support of NIH Grant No. 850RR05651A.

[1] F. H. Stillinger, J. Chem. Phys. **78**, 4654 (1983).
[2] D. Wu, D. Chandler, and B. Smit, J. Phys. Chem. **96**, 4077 (1992).
[3] M. W. Deem and D. Chandler, preceding paper, Phys. Rev. E **49**, 4268 (1994).
[4] See, for example, M. Teubner and R. Strey, J. Chem. Phys. **87**, 3195 (1987); D. Roux, C. Coulon, and M. E. Cates, J. Phys. Chem. **96**, 4174 (1992); G. Gompper and S. Klein, J. Phys. (Paris) II **2**, 1725 (1992).
[5] G. Gompper and M. Kraus, Phys. Rev. E **47**, 4289 (1993); **47**, 4301 (1993).
[6] J. W. Cahn, J. Chem. Phys. **42**, 93 (1965).
[7] N. F. Berk, Phys. Rev. Lett. **58**, 2718 (1987); S. H. Chen, S. L. Chang, and R. Strey, J. Appl. Cryst. **24**, 721 (1991); S. Marčelja, J. Phys. Chem. **94**, 7259 (1990); P. Pieruschka and S. Marčelja, J. Phys. (Paris) II **2**, 235 (1992).
[8] M. Teubner, Europhys. Lett. **14**, 403 (1991).
[9] T. Ohta, D. Jasnow, and K. Kawasaki, Phys. Rev. Lett. **49**, 1223 (1982); Y. Oono and S. Puri, Mod. Phys. Lett. B **2**, 861 (1988); G. F. Mazenko, Phys. Rev. B **42**, 4487 (1990).
[10] R. P. Feynman, *Statistical Mechanics: A Set of Lectures*, (Addison-Wesley, New York, 1972), Secs. 2.11 and 3.4.
[11] W. H. Press, B. P. Flannery, S. A. Teukolsky, and W. T. Vetterling, *Numerical Recipes in Fortran*, 2nd ed. (Cambridge University Press, New York, 1992), Sec. 9.7.
[12] W. H. Press *et al.*, *Numerical Recipes in Fortran* (Ref. [11]), Sec. 4.5.
[13] D. Chandler, *Introduction to Modern Statistical Mechanics* (Oxford University Press, New York, 1987), Sec. 7.2.
[14] W. Jahn and R. Strey, J. Phys. Chem. **92**, 2294 (1988).
[15] E. Caponetti, A. Lizzio, and R. Triolo, Langmuir **6**, 1628 (1990).
[16] K.-V. Schubert and R. Strey, J. Chem. Phys. **95**, 8532 (1991).
[17] L. Auvray, J.-P. Cotton, R. Ober, and C. Taupin, J.

Phys. Chem. **88**, 4586 (1984).
[18] S. H. Chen, S. L. Chang, and R. Strey, J. Appl. Cryst. **24**, 721 (1991).
[19] J. S. Rowlinson and B. Widom, *Molecular Theory of Capillarity* (Oxford University Press, Oxford, 1982), Sec. 3.1.
[20] R. C. Weast, *CRC Handbook of Chemistry and Physics*, 68th ed. (CRC Press, Boca Raton, FL, 1987), p. F-34.
[21] W. H. Press *et al.*, *Numerical Recipes in Fortran* (Ref [11]), Sec. 12.5.
[22] R. Strey, R. Schomäcker, D. Roux, F. Nallet, and U. Olsson, J. Am. Chem. Soc. Faraday Trans. **86**, 2253 (1990).

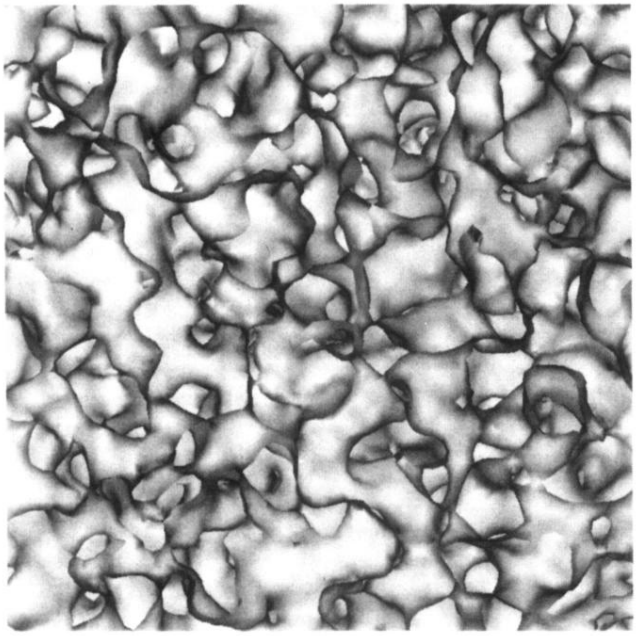

FIG. 5. The three-dimensional level surface $\rho_1(\mathbf{r}) - \rho_4(\mathbf{r})$ is visualized for the second parameter set of Table II. The view is along the z axis of a $64 \times 64 \times 64$ grid with 30 Å resolution.